Chalcogenide Letters Vol. 21, No. 9, September 2024, p. 729 - 746

Electrochemical analysis on $SnSeO_3/ZnSeO_3$ nanocomposite

N. G. Basil Ralph[a], S. Shanmugha Soundare[b], D. Yamuna[a], S. Ariponnammal[a,*]
[a]*Department of Physics, Gandhigram Rural Institute, Deemed To Be University, Gandhigram-624302, Dindigul District, Tamilnadu, India*
[b]*Centre for Nanoscience and Technology, Anna University, Chennai-600025, Tamilnadu, India*

Nanocomposite $SnSeO_3/ZnSeO_3$ has been synthesized by hydrothermal method. X-ray powder diffraction confirms formation of $SnSeO_3/ZnSeO_3$ nanocomposite. It exhibits an interesting morphology of needle like nanorod structure. Thermal analysis reveals the thermal stability, decomposition behavior and critical temperatures where significant weight loss occurs. X-ray photoemission explains the role of the chemical state Sn, Zn, Se and O in $SnSeO_3/ZnSeO_3$. Electrochemical study has been made in both three electrode and two electrode system. In three electrode system, cyclic voltammetry exhibits a bell-shaped curve and the operational potential window is 0.8 V. The specific capacitance is 78.65 F/g for 5 mV scan rate. Chronopotentiometry shows quasi-triangular curves demonstrating the behavior of pseudo capacitors. Specific capacitances of 72.02 F/g was delivered at 1 A/g current density in 3M electrolyte of KOH. The plot of Nyquist for $SnSeO_3//ZnSeO_3$ confirms pseudo capacitor behavior. The series resistance Rs is low that is 0.78 Ω and charge transfer resistance is 0.42 Ω. Symmetric $SnSeO_3/ZnSeO_3$ supercapacitor device that is, two electrode system, is fabricated using 3M KOH electrolyte. Operational potential window is 1.5V. Cyclic voltammetry curves of the device show excellent capacitive behavior. The symmetric device produced specific capacitances of 39.37F/g, energy density 6.15 Wh kg^{-1} and power density 374.99 kW kg^{-1} at 1Ag^{-1} current density. The cell displayed 73.18% capacity retention, indicating excellent electrode stability for approximately 5000 cycles at a current density of 1 Ag^{-1}. Nyquist plot suggests that the system is stable and exhibits capacitive behavior.

(Received April 24, 2024; Accepted September 16, 2024)

Keywords: $SnSeO_3/ZnSeO_3$, Nanocomposite, Thermal, X-ray photoemission, Electrochemical studies

1. Introduction

The universe needs clean, renewable energy storage technology to maintain a pollution free atmosphere. The production of energy storage devices with great efficiency, has garnered significant interest owing to the growing need for renewable energy sources. Supercapacitors (SCs) are

* Corresponding author: ariponnammal@gmail.com
https://doi.org/10.15251/CL.2024.219.729

regarded as the most promising energy storage technology.

They are electrochemical capacitors that are a potential SCs new class of energy storage devices in terms of power density, energy density, longevity, and safety tolerances. Recently, there has been a significant focus on thin and flexible SCs in order to address the increasing need for portable electronic gadgets. It is required to locate suitable electroactive materials and incorporate them into certain device architectures for these applications. In order to improve the power density and cycling stability of SCs, active materials with tubular or layered structures, as well as hierarchical pores, can encourage charge transport and ion diffusion. Furthermore, energy storage devices made of certain pseudocapacitive materials is influenced by their phase and composition. A variety of nanostructured materials have been created, to produce SCs with desired qualities.

These materials include carbon nanotubes, graphene and its composites, layered hydroxides and oxides, and metal-oxide hybrids. A two-dimensional metal chalcogenide is important functional nanomaterials with distinctive electronic composition and physical properties, due to their special geometric structures, variable composition, rich phase structure, and weak interlayer Van de Waals coupling. Consequently, they offer an enormous material for flexible energy storage devices. However, the only active materials utilized in flexible SCs are VS_2 nanosheets. Numerous bimetallic selenides were investigated as potential materials for supercapacitor applications. Zinc selenide, which has two distinct crystal structures of zinc blende cubic and wurtzite hexagonal, is used in diode lasers and light emitting diodes. Tin selenide crystallizes into two primary phases of orthorhombic SnSe and hexagonal $SnSe_2$. Tin selenides, a layered metal chalcogenide, are narrow band gap semiconductors that find applications as anode materials for solar cells, memory switching devices, lithium ion batteries, and infrared optoelectronic devices. However, these materials frequently run into phase or composition related problems during their synthesis. Nowadays, metal oxides and conducting polymers are examined as materials for electrode in supercapacitors. Conducting polymers lack mechanical strength and cycling stability, but metal oxides are readily available, have a range of oxidation states, and have a high specific capacitance [1]. Materials with imperfections can also be used for energy storage, batteries, photocatalysis, electrocatalysis, and thermal catalysis. In nature, metal oxides are prevalent and chemically stable. They are inexpensive and have distinctive electronic architecture.

The presence of imperfections favours the materials. Because, photo catalysis, energy storage, and electro catalysis all significantly depend on oxygen vacancy [2-3]. It is interesting to study oxy chalcogenides or for example selenite which includes oxygen. Despite these, there have been no published investigations on the analysis of Zinc and Tin Selenites of super capacitors. Therefore, in this paper the doping effect of Tin in place of Zinc is studied. In other words, the nanocomposite $SnSeO_3/ZnSeO_3$is synthesized and thorough study has been made and reported in this paper.

2. Methods and materials

The nanocomposite $SnSeO_3/ZnSeO_3$ was synthesized by one pot hydrothermal technique [4]. The sample is characterized by scanning electron microscopy (SEM), X-ray powder diffraction (XRD), thermal analysis, electrochemical analysis and X-ray photo emission spectroscopy. The England made OXFORD INCAPENTAx3 model is used for recording EDAX, the Carel ZEISS

EVO-18 model for recording SEM, Panalytical X'Pert Pro model for recording XRD with Cu Kα radiation, Thermo Fisher Scientific's XPS device for recording XPS spectra using Al Kα radiation (1486.6 eV), thermal analysis by NETZSCH make NJA-STA2500 Regulus model with Proteus software in the temperature range of 30° to 800° C and Bio-Logic VSP potentiostat model for doing electrochemical experiments.

The electrochemical performance of the synthesized $SnSeO_3/ZnSeO_3$ electrode was evaluated in a three-electrode cell arrangement. A mixture of $SnSeO_3/ZnSeO_3$, carbon black, and PVDF was taken in a mortar and pestle and mixed well with a few drops of NMP solution (N-methyl pyrrolidone) in order to evaluate the electrochemical performance of $SnSeO_3/ZnSeO_3$. This slurry mixture was then applied to a 1 cm^2 Ni foam, which was then dried. In this work, 3M KOH electrolyte was utilized. Here, platinum wire serves as the counter electrode, Ag/AgCl serves as the reference electrode, and Ni foam coated with substance serves as the working electrode.

3. Results and discussion

3.1. XRD

Figure 1 depicts XRD of $SnSeO_3/ZnSeO_3$ nano composite. Indexing of Peaks are made. Lattice parameters are a = 6.350 Å, b = 8.224 Å, and c = 5.852 Å [4] for $SnSeO_3$ and a=5.14 Å, b = 6.00 Å, and c = 7.81 Å for $ZnSeO_3$ [5]. Both are of structure orthorhombic. Disappearance of alloy peaks and peaks shifts confirmed the formation of nano composite $SnSeO_3/ZnSeO_3$ [6].

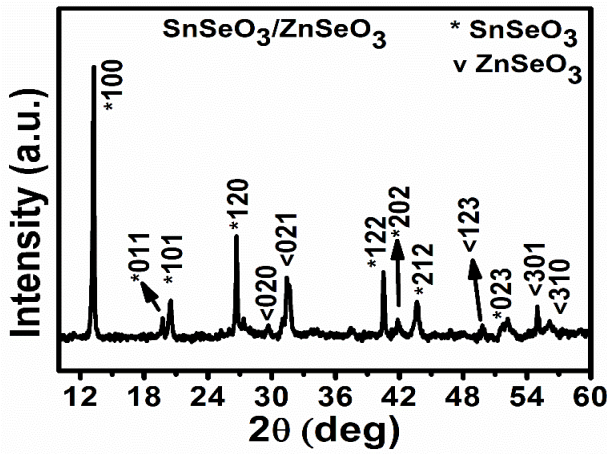

Fig. 1. XRD of $SnSeO_3/ZnSeO_3$ nanocomposite.

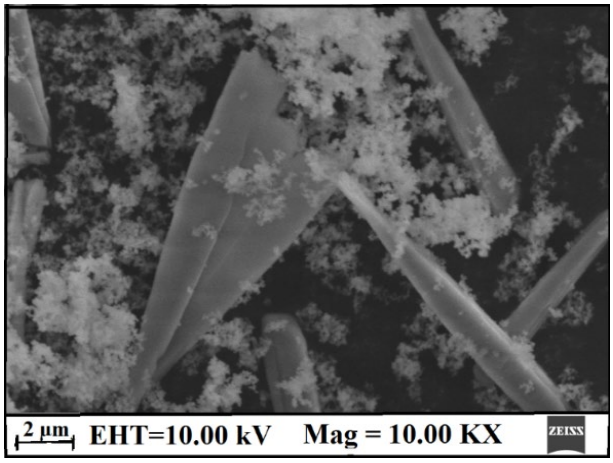

Fig. 2. SEM image of $SnSeO_3$/$ZnSeO_3$ nanocomposite.

3.2. Surface morphological studies

Figure 2 depicts SEM picture of $SnSeO_3$ /$ZnSeO_3$ at 10 KX magnification. It exhibits sharp needle like nano rod structure.

3.3. Thermogravimeric analysis (TGA)

Figure 3 shows TGA curve of $SnSeO_3$ /$ZnSeO_3$.The TGA curve represents the percentage of weight remaining as the sample when heated. The x-axis corresponds to temperature (in degrees Celsius), ranging from approximately 50°C to nearly 800°C [7]. The left y-axis shows TG (%), indicating how much percentage of mass remains as temperature increases with values range from 65% to 100%. It has been observed that 3.16% mass change occurs around 200°C, 9.82% mass change occurs around 350°C and a mass change of 24.36% occurs with temperature increase from 350°C to 800°C. The total mass change occurred is about 37.34% [8]. The differential thermo gravimetric (DTG) curve represents the rate of weight loss per minute as a function of temperature. Peaks observed in DTG curve are corresponding to temperatures where there is a significant change in the rate of mass loss. These peaks indicate rapid weight loss associated with specific thermal events such as decomposition and phase transitions etc. [9]. The TGA curve reveals the thermal stability and decomposition behaviour of the sample. The DTG peaks highlight critical temperatures where significant weight loss occurs. The overall pattern suggests multiple stages of decomposition or volatilization [10-11].

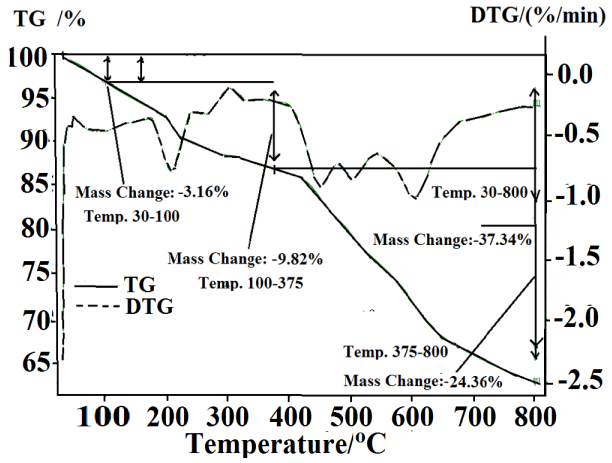

Fig. 3. TGA curve of $SnSeO_3/ZnSeO_3$ nanocomposite.

3.4. Differential thermal analysis (DTA)

Figure 4 shows DTA curve of $SnSeO_3$ /$ZnSeO_3$. The x-axis represents temperature in degrees Celsius (°C). The range extends from 0°C to 800°C. The y-axis represents heat flow in microvolts per milligram (µV/mg). Heat flow indicates the energy exchange either absorbed or released, during a thermal process. At lower temperatures upto approximately 100°C, the curve remains relatively flat with minor fluctuations. This suggests no significant thermal events during this range [12]. There are three peaks observed at 210°, 250° and at 290°C. The peak at 210° likely corresponds to a thermal event in the sample which may be due to phase transition, such as crystallization or polymorphic transformation. It may also be due to chemical reaction due to the occurrence of decomposition, oxidation etc.

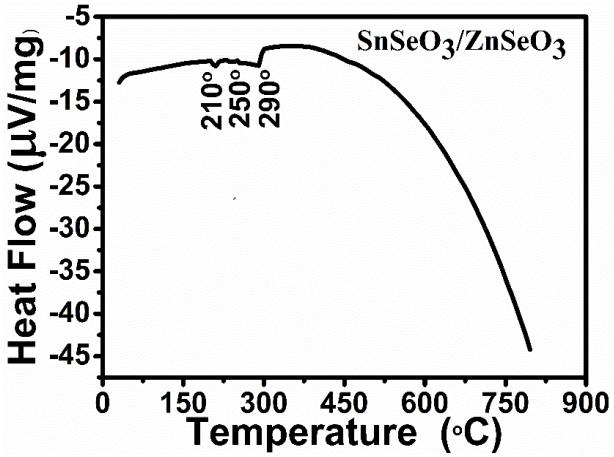

Fig. 4. DTA curve of $SnSeO_3/ZnSeO_3$ nanocomposite.

The peak at 250°C signifies a significant change. Suppose, if the sample contains crystalline regions, this could be the melting point. It might also indicate other transitions such as glass transition and recrystallization. The peak at 290°C could be another phase transition e.g., solid-solid

transition or it may be any chemical reactions occur at this temperature. Beyond this peak, the curve gradually slopes downward. This suggests an endothermic process where the sample absorbs heat by melting or decomposition. The DTA graph provides insights into material behaviour under varying temperatures. The exothermic peak reveals important transition points, which can be useful for material characterization [13].

3.5. X-ray photo emission spectroscopy

Figure 5 shows tin 3d scan of $SnSeO_3$ /$ZnSeO_3$. The peak at lower binding energy around 487.93 eV corresponds to the Sn $3d_{5/2}$ orbital. It represents the energy required to remove an electron from the 3d subshell of tin atoms. The position of this peak provides information about the chemical environment of tin in the material. The peak at higher binding energy around 496.36 eV corresponds to the Sn $3d_{3/2}$ orbital. Like the $3d_{5/2}$ peak, it also reflects the tin's chemical state. The relative intensity and separation between these two peaks can reveal oxidation states or bonding configurations.

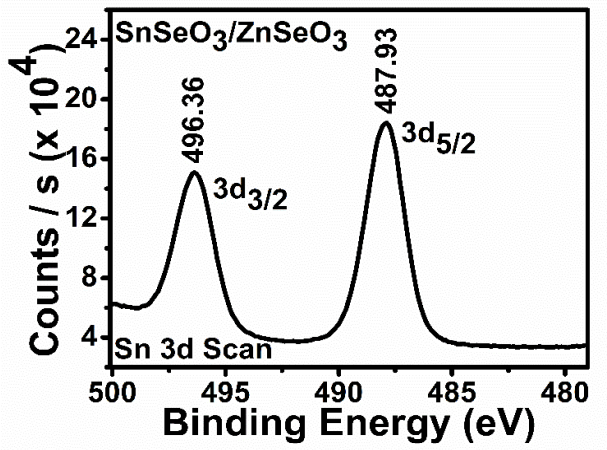

Fig. 5. Tin 3d scan of $SnSeO_3$ /$ZnSeO_3$.

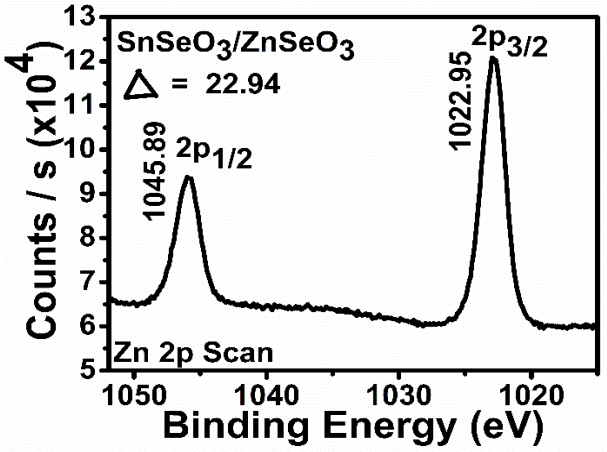

Fig. 6. Zinc 2p scan of $SnSeO_3$ /$ZnSeO_3$.

The spectrum is relevant for analysing the surface chemistry of a specific material $SnSeO_3/ZnSeO_3$. This material could be a layered compound or a composite containing both tin selenite and zinc selenite. The XPS peaks help to characterize the tin atoms in this compound [14].

Figure 6 shows Zinc 2p scan of $SnSeO_3/ZnSeO_3$. XPS explains the role of the Zn chemical state in $SnSeO_3/ZnSeO_3$. The peaks in the zinc scan corresponds to Zinc (Zn) at its 2p energy level. The binding energy of the peaks provides information about the Zn oxidation state. The higher intensity suggests a significant presence of Zn in the material. The Zn 2p peak corresponds to the binding energy of zinc's 2p electrons. It typically shows two spin-orbit components: Zn $2p_{3/2}$ and Zn $2p_{1/2}$. The Zn $2p_{3/2}$ peak is centred on 1022.95 eV. The Zn $2p_{1/2}$ peak is slightly higher in binding energy 1045.89 eV. The spin-orbit splitting between these components (Δ metal) is approximately 22.94 eV [1]. It has been reported that Zinc oxide shows peaks at 1022.25 and 1045.31 eV [14-15], confirming the existence of a Zn oxide matrix in the sample [16].

The Figure 7 depicts Se 3d spectrum confirms Se (II) presence by the occurrence of $3d_{5/2}$ and $3d_{3/2}$peaks at BEs of 56.39 and 60.43 eV with a split of spin-orbit 4.04eV, which is consistent with literature for Se in a selenite (SeO_3) state [17]. The position and shape of this peak provide information about the chemical environment of selenium in the sample. The binding energy of each sub peak provides insights into the oxidation state of selenium [17].

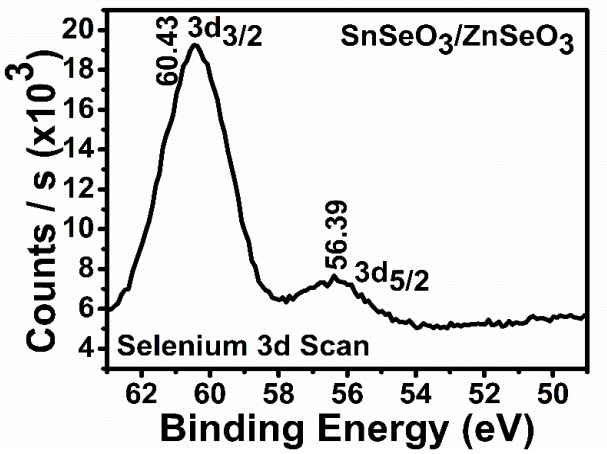

Fig. 7. Selenium 3d scan of $SnSeO_3$ /$ZnSeO_3$

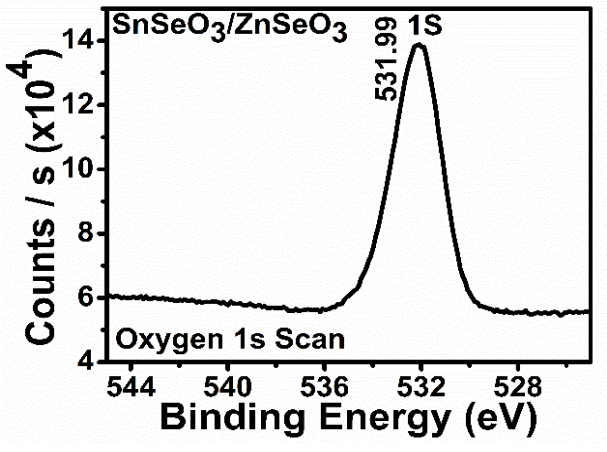

Fig. 8. Oxygen 1s scan of $SnSeO_3$ /$ZnSeO_3$.

The most prominent peak in oxygen scan (Figure 8) occurs around 531.99 eV. This peak corresponds to the oxygen 1s core level signal. The "1s" refers to the innermost electron shell of oxygen atoms. The peak position provides information about the chemical environment of oxygen in the material. Different chemical states such as oxides, hydroxides, or adsorbed species exhibit distinct oxygen 1s peaks. It has been reported that metal oxides bonds exhibit peaks around 529 – 530 eV [14]. The oxygen 1s peak at binding energy 531.99 eV, suggesting the production of a metal oxide bond that is oxides of Tin and Zinc [18].

3.6 Electrochemical performance in three electrode configurations

3.6.1 Cyclic voltammetry (CV)

Cyclic voltammetry plot of $SnSeO_3$//$ZnSeO_3$ nano composite, exhibits a typical bell-shaped curve as in Figure 9 and operational potential window of 0.8 V for various scan rates 5 mV, 10 mV, 25 mV, 50 mV, 75 mV and 100 mV. The specific capacitance values obtained from CV plot are 78.65 F/g, 63.87 F/g, 50.85 F/g, 44.43 F/g, 40.94 F/g and 38.50 F/g. Specific capacitance reduces with increasing scan rate as in Figure 10 due to electrode-electrolyte interaction [19-21].

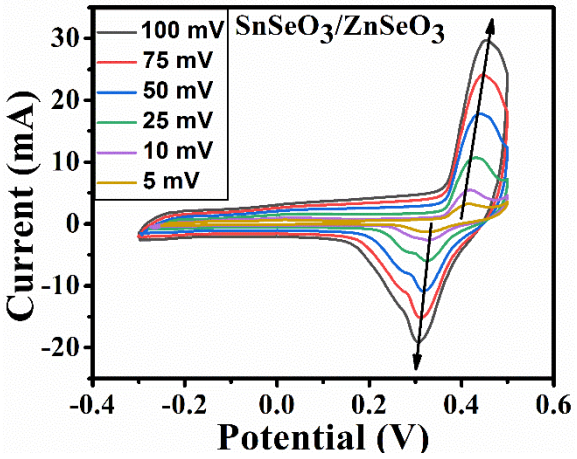

Fig. 9.CV curves $SnSeO_3$ /$ZnSeO_3$.

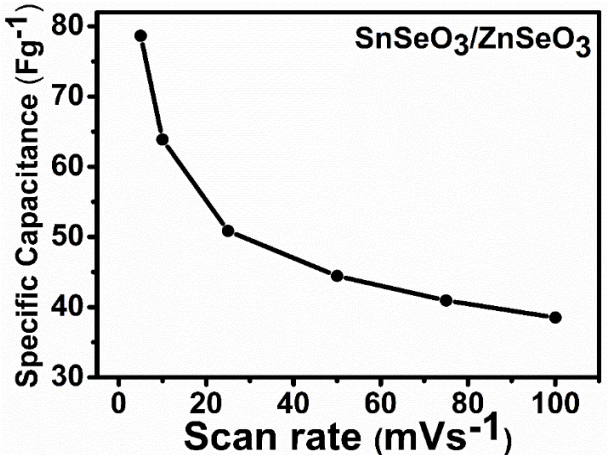

Fig. 10. Specific capacitance versus scan rate $SnSeO_3$ /$ZnSeO_3$.

As the scan rate changes, the peak currents and potentials shift. The adsorption of cations in the electrolyte on an electrode surface is the mechanism responsible for charge storage. The electrostatic adsorption of ions is responsible for oxidation peak potential rise and reduction peak potential fall with scan speeds 5, 10, 25, 50, 75, and 100 mV/s. It results from the redox reaction governed by the kinetics of charge transfer. Due to insufficient ion intercalation into the dense centre of the nanostructure, anodic peaks shift to higher potential and cathodic peaks to lower potential. Redox peak shift indicates the electrode material's good rate capacity for supercapacitor applications [22]. On observing the peaks in the curve, the anodic peak corresponds to oxidation representing electron loss, while the cathodic peak corresponds to reduction representing electron gain. The position of these peaks provides insights into the material's redox behaviour. At slow scan rates, the process is diffusion-limited controlled by mass transport. At fast scan rates, the process becomes kinetics-limited controlled by reaction kinetics [23].

At slow scan rates, the electrochemical process is primarily influenced by mass transport. The diffusion layer around the electrode grows more extensively. Consequently, the flux of electro active species of ions or molecules reaching the electrode surface is considerably smaller. When the scan rate is slow, the reactants that is, ions or molecules have sufficient time to diffuse to the electrode surface. Slower scan rates allow more time for mass transport or diffusion of ions or molecules to the electrode surface. However, this extended time doesn't necessarily lead to higher capacitance [24]. The limiting factor is how quickly they can move through the solution to reach the electrode. The slower diffusion of ions results in lower charge storage capacity, the extended diffusion time allows ions to accumulate near the electrode, as a result, the effective surface area for charge storage increases when more ions are near the surface. Therefore, the specific capacitance normalized by surface area tends to be higher. The current response that is, peak current is directly related to the rate of mass transport. Diffusion-limited processes often exhibit well-defined, symmetric peaks in CV curves. The system behaves closer to the diffusion-limited regime. At fast scan rates, the electrochemical process becomes dominated by reaction kinetics. When the scan rate is fast, the reactants don't have enough time to fully participate in the redox reaction [25]. The limiting factor is how quickly the electrons can transfer between the electrode and the reactants. At faster scan rates, the diffusion layer remains thinner. The flux of species to the electrode surface increases. Peak currents of both anodic and cathodic become larger. Faster scan rates enhance charge transfer kinetics. The system behaves closer to the kinetics-limited regime. Rapid electron transfer allows for higher charge storage capacity. However, the specific capacitance may decrease due to limited time for ion diffusion. Peaks may appear sharper due to rapid electron transfer. The current response of peak current is now influenced by the kinetics of the redox process [26].

3.6.2. Galvanostatic charge-discharge analysis (GCD)

Figure 11 illustrates chronopotentiometry (CP) analysis of charging and discharging at current densities 1, 2, 3, 4, 5 and 6 A/g for $SnSeO_3/ZnSeO_3$ in 3M KOH electrolyte. Quasi-triangular CP curves demonstrate the behaviour of pseudo capacitors. The internal resistance of the electrode material increases with an increase in current density [27-28].

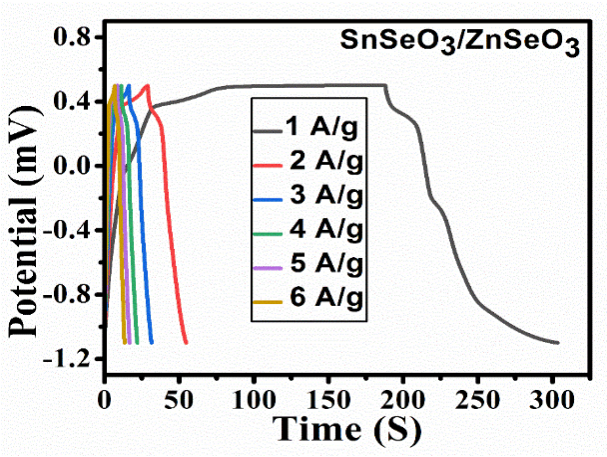

Fig. 11. GCD curves $SnSeO_3$ /$ZnSeO_3$.

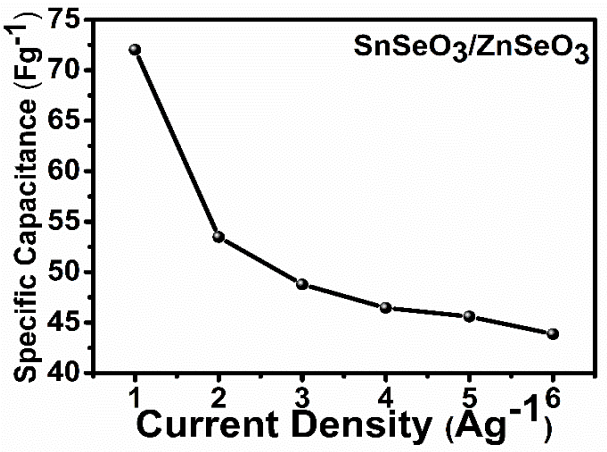

Fig. 12. Specific capacitance versus current density of $SnSeO_3$ /$ZnSeO_3$ from GCD.

In fact, the material-specific capacitance is proportional to the active surface area engaged in electrode-electrolyte interactions. Specific capacitances of 72.02, 53.47, 48.78, 46.45, 45.59 and 43.86 F/g were delivered (Figure 12) for 1, 2, 3, 4, 5 and 6 A/g current densities in 3M electrolyte of KOH, respectively, using $SnSeO_3$/$ZnSeO_3$. At low current densities, the charge transfer kinetics dominate. The electrode reactions oxidation or reduction occur more slowly. The potential response reflects this sluggish behaviour. At higher current densities, faradaic processes become more significant. These involve reversible redox reactions at the electrode surface. Pseudo capacitance contributes to the overall capacitance. If the supercapacitor material exhibits pseudo capacitance, additional redox reactions occur. These faradaic processes contribute to the overall capacitance [29]. The plateau may be more pronounced if pseudo capacitance is significant. These reactions occur faster at higher currents. Beyond a certain voltage, the capacitance reaches a plateau. Adding more voltage doesn't significantly increase the charge storage capacity. Faradaic reactions have limits, and their contribution saturates [30]. The potential stabilizes due to the balance between charge transfer and ion diffusion. At high currents, ion diffusion becomes challenging. The ions have less

time to reach the electrode surface. Diffusion limitations affect the rate of charge storage. Specific capacitance decreases at a high value of current densities. This imply that the trapping of ions required for electrochemical behaviour, gets lacking and the activation sites are less for electrolytic ions at interface of electrode-electrolyte [31].

3.6.3. Nyquist plot

Figure 13 illustrates a plot of Nyquist for $SnSeO_3$//$ZnSeO_3$ with expanded plot as an inset. It shows semicircle with the Warburg region continues to extend, confirms pseudo capacitor behaviour. A very small semicircle represents charge-transfer process. The series resistance Rs is low that is, 0.78 Ω and charge transfer resistance is 0.42 Ω. The equivalent circuit model called Randles circuit is drawn as an inset. It can be used to describe electrode processes when both kinetics and diffusion are non-negligible. The solution resistance (RΩ), a psuedo capacitor (C), the charge transfer resistance, and Warburg element *Z*WAR containing information on the species' diffusion coefficient are all included [32-35].

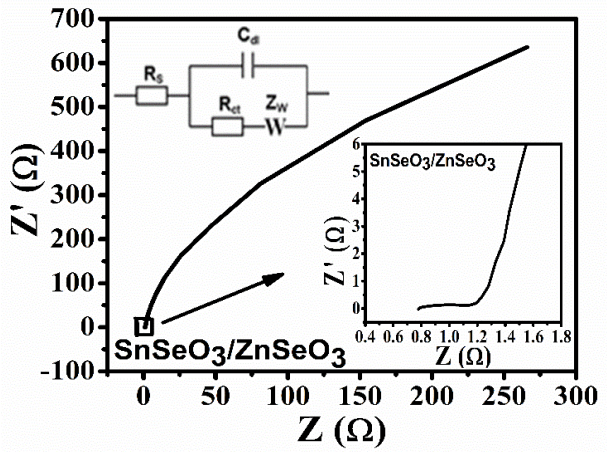

Fig. 13. Nquist plot of $SnSeO_3$ /$ZnSeO_3$ in three electrode system.

3.7. Fabrication of $SnSeO_3$/$ZnSeO_3$ based Symmetric Supercapacitor Device

For a real-world application, a symmetric $SnSeO_3$/$ZnSeO_3$ supercapacitor device (two electrode system) is created using 3M KOH electrolyte. The total amount of active ingredient in the device was about 6 mg. Here, a polyurethane foam separator was employed to keep the working electrodes from coming into direct touch with one another. To assemble the device, two identical 1 × 1 cm^2 $SnSeO_3$/$ZnSeO_3$ Nickel foam electrodes with equivalent weights were placed face-to-face. After being immersed in 3M KOH electrolyte, the separator Polyurethane foam was covered with adhesive tape. Following cell assembly, a sandwich-like matrix with two symmetric electrodes was created by injecting KOH electrolyte into the separator between the positive and negative electrodes. For the purpose of creating a symmetric supercapacitor, the mass ratio of the positive to the negative electrode was balanced based on the three electrodes' performance. The symmetric supercapacitor device uses two identical $SnSeO_3$/$ZnSeO_3$ /NF electrode materials as the cathode and anode.

3.7.1. CV response of the device

Figure 14 illustrates the cyclic voltammetry performance of the symmetric supercapacitor device at various scans, ranging from 5 to 100 mV/s. Operational potential window is 1.5V between 0 and 1.5V.

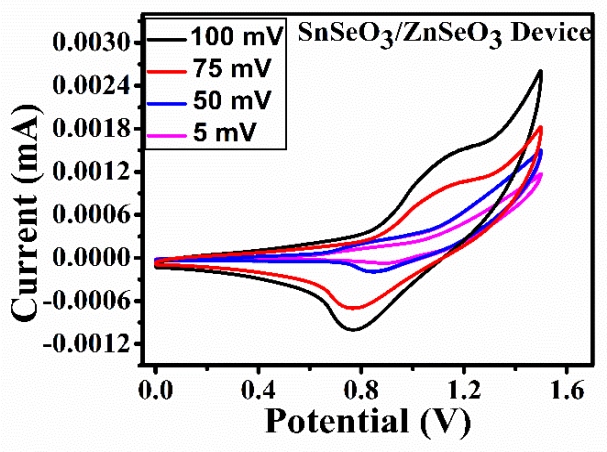

Fig. 14.CV curves $SnSeO_3$ /$ZnSeO_3$ device.

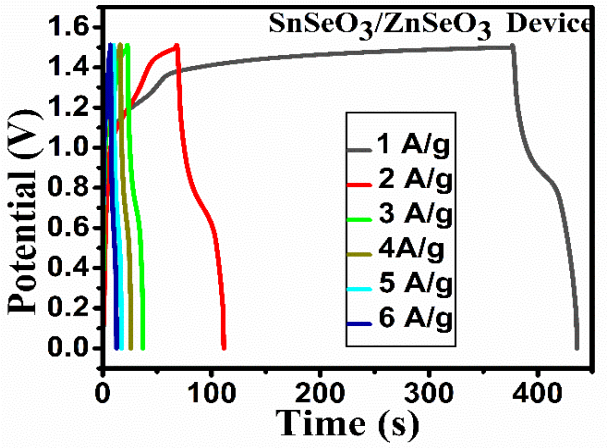

Fig. 15.GCD curves $SnSeO_3$ /$ZnSeO_3$ device.

The CV curves of all symmetric devices show excellent capacitive behaviour, performing consistently even at high scan rates. Furthermore, because the total current is linearly proportional to the scan rate, it is evident that it grows as the scan rate increases. Even at high scan rates, there was no significant distortion of the cyclic voltammograms' form, suggesting that a sizable portion of the $SnSeO_3$-$ZnSeO_3$ nanocomposite device electrode surfaces' inner region contributed to the capacitance. These findings supported earlier research on $SnSeO_3$/$ZnSeO_3$ electrodes measured in a three-electrode cell configuration, which demonstrated the symmetric supercapacitor's superior electrochemical reversibility. The shape of the CV curves showed a similar pattern with increased scan speeds, suggesting high reversibility.

3.7.2. Chronopotentiometry (CP)

Galvanostatic charging-discharging (GCD) experiments were carried out as shown in Figure15 to confirm the better electrochemical performance of the $SnSeO_3$-$ZnSeO_3$ symmetric supercapacitor device using a current density varying from 1 to 6 A/g and a constant potential of 1.5 V. The electrode materials' discharge time is prolonged by the greater voltage of 1.5 V, which also ensures good columbic efficiency and highlights the materials' enormous potential for energy storage. Additionally, as a result of redox reactions, the charge-discharge curves show a slight divergence from a linear shape. The figure 15 illustrates that all GCD curves are roughly symmetrical and have a distinct plateau region that signifies low internal resistance faradaic reactions for charge/discharge operations without any discernible internal ohmic (iR) drop [36-38]. At current densities of 1, 2, 3, 4, 5, and 6 Ag^{-1}, respectively, the symmetric device produced specific capacitances of 39.37, 34.93, 28.66, 25.44, 24.58, and 22.29 Fg^{-1} in 3M KOH. Rapid potential shifts at higher current densities limit the ability of ions to permeate into the inner region of the electrode surface by causing a decrease in specific capacitance. At lower current densities, a slower potential change and more time for the ions to be adsorbed at the electrode surface translate into a greater specific capacitance value. The estimated specific capacitance value was plotted against the current density, as shown in Figure 16. Furthermore, the energy density and power density of supercapacitors two critical parameters were determined. The symmetric supercapacitor demonstrated a significant retention of energy density with an increase in power density [39]. Table1 displays the specific capacitance, energy density, and power density from CP. The Ragone graph depicted in Figure 17 contrasts the electrochemical supercapacitor's energy density and power density, to evaluate a supercapacitor. It demonstrates how current density causes an increase in power density and a decrease in energy density. Capacity to store charge is known as energy density. A decrease in active surface area results in a rise in current density. Lower energy density at increasing current densities is the consequence of this decrease in stored total charge. The charge-discharge curve shape that is maintained at all sweep rates further validates $SnSeO_3$/$ZnSeO_3$ as an active material that can be used for energy storage.

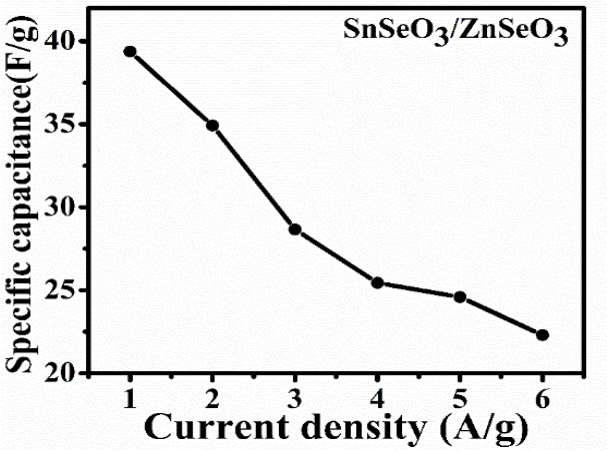

Fig. 16. Specific capacitance versus current density from GCD curves of $SnSeO_3$ /$ZnSeO_3$ device.

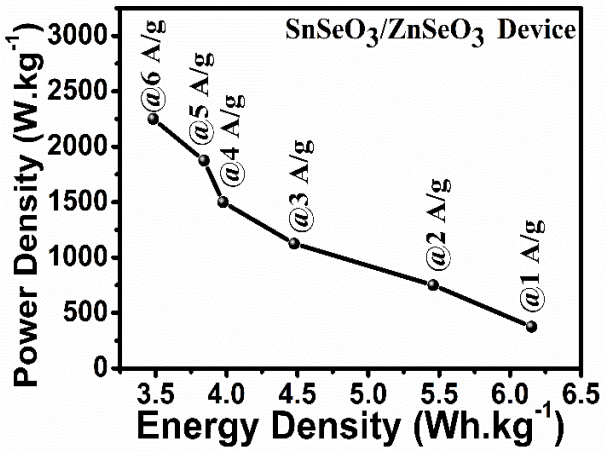

Fig. 17. Ragone's plot of $SnSeO_3$ /$ZnSeO_3$ device

Table 1. Specific capacitance, energy density, and power density of $SnSeO_3$/$ZnSeO_3$ device.

Current Density(A/g)	**Specific Capacitance (F/g)**	**Energy Density (Wh kg^{-1})**	**Power Density (kW kg^{-1})**
1	39.37	6.150	374.99
2	34.93	5.460	749.99
3	28.66	4.480	1125.00
4	25.44	3.970	1500.00
5	24.58	3.840	1875.00
6	22.29	3.480	2250.00

3.7.3. Cyclic stability

A longer electrochemical cycle life is a critical need for supercapacitor devices. The cycle life span of the $SnSeO_3$/$ZnSeO_3$ positive and negative electrodes of the manufactured symmetric cell was analysed for potential practical uses. The $SnSeO_3$/$ZnSeO_3$ sample needed some time to reach its maximum specific capacitance. After that, its wettability helped to increase ionic mobility at the electrode-electrolyte interface, and in the end, the cell displayed in Figure 18, an impressive 73.18% capacity retention, indicating excellent electrode stability for approximately 5000 cycles at a current density of 1 Ag^{-1}.

3.7.4. Nyquist plot

A Nyquist plot with a slanting line and no semicircle typically indicates that the system has no poles or zeros in the right-half plane (RHP). Poles in the RHP would cause the Nyquist plot to encircle the origin that is forming a semicircle. No semicircle suggests that the system is stable since no poles are in the RHP. The slanting line represents the contribution from the poles and zeros in the left-half plane. If the system corresponds to a physical process such as electrical circuit or mechanical system, this behaviour indicates stability [40-41]. Typically, Nyquist plots exhibit semicircles due to the presence of poles and zeros in the system. A semicircle corresponds to the

impedance response associated with a specific relaxation process such as charge transfer at an electrode interface. The observed slanting line (Figure 19) suggests that there are no significant relaxation processes such as capacitive behaviour within the probed frequency range. This behaviour could be due to the absence of specific interfaces or surface reactions.

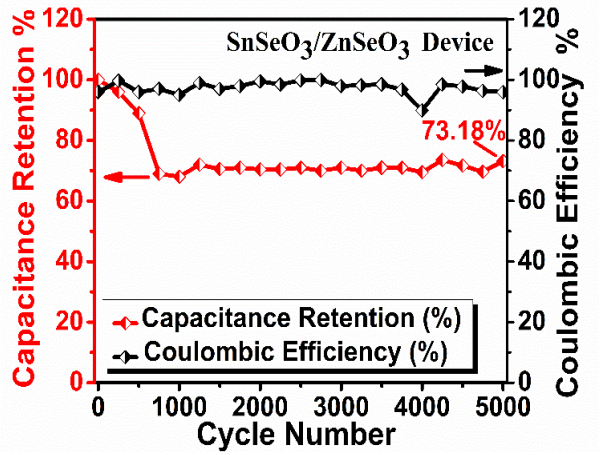

Fig. 18. Cyclic stability of $SnSeO_3$ /$ZnSeO_3$ device.

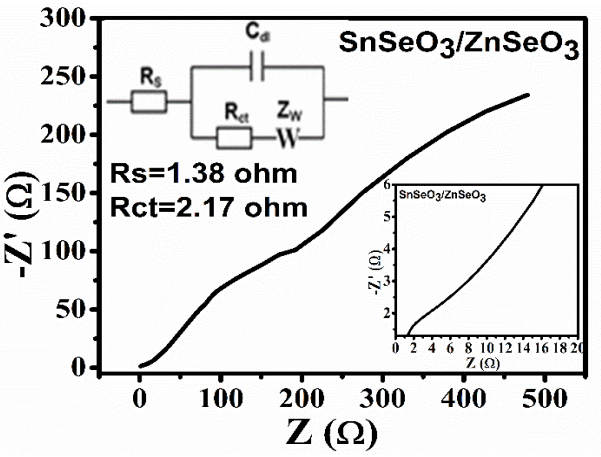

Fig. 19. Nyquist plot of $SnSeO_3$ /$ZnSeO_3$ device.

If this nano composite has a uniform conductivity throughout, it may result in a simple linear response. The slanting line could indicate bulk conductivity that is electronic conduction within the material [42-43]. The series resistance Rs is low that is, 1.38 Ω and charge transfer resistance is 2.17 Ω. The equivalent circuit model called Randles circuit is drawn as an inset.

4. Conclusions

Nanocomposite $SnSeO_3/ZnSeO_3$ has been synthesized by hydrothermal method. XRD confirm the perfect formation of $SnSeO_3/ZnSeO_3$ nano composite. It shows an interesting morphology of needle like nano rod. TGA curve reveals the thermal stability and decomposition behaviour of the sample. The DTG peaks highlight critical temperatures where significant weight loss occurs. The overall pattern suggests multiple stages of decomposition or volatilization. The DTA graph provides insights into material behaviour under varying temperatures useful for material characterization. XPS explains the role of the chemical state Sn, Zn, Se and O in $SnSeO_3/ZnSeO_3$. Electrochemical study was made in both three electrode and two electrode system. In three electrode system, cyclic voltammetry plot of $SnSeO_3/ZnSeO_3$ nano composite, exhibits a typical bell-shaped curve and operational potential window of 0.8 V.

The specific capacitance values from CV plot are 78.65 F/g, 63.87 F/g, 50.85 F/g, 44.43 F/g, 40.94 F/g and 38.5 F/g for various scan rates 5 mV, 10 mV, 25 mV, 50 mV, 75 mV, and 100 mV. Chronopotentiometry (CP) analysis of charging and discharging shows quasi-triangular curves demonstrate the behaviour of pseudo capacitors. Specific capacitances of 72.02, 53.47,0 48.78, 46.45, 45.59 and 43.86 F/g were delivered for 1, 2, 3, 4, 5 and 6 A/g current densities in 3M electrolyte of KOH, respectively, using $SnSeO_3/ZnSeO_3$.The plot of Nyquist for $SnSeO_3//ZnSeO_3$ confirms pseudo capacitor behaviour. The series resistance Rs is low that is, 0.78 Ω and charge transfer resistance is 0.42 Ω. Symmetric $SnSeO_3/ZnSeO_3$ supercapacitor device of two electrode system is fabricated using 3M KOH electrolyte. It exhibits the operational potential window is 1.5V.

The CV curves of symmetric device show excellent capacitive behaviour. The symmetric device produced specific capacitances of 39.37F/g, energy density 6.15Wh kg^{-1} and 374.99 $kWkg^{-1}$ at $1Ag^{-1}$ current density. The cell displayed 73.18% capacity retention, indicating excellent electrode stability for approximately 5000 cycles at a current density of 1 Ag^{-1}. Nyquist plot suggests that the system is stable and exhibits capacitive behaviour. Series resistance Rs is low that is, 1.38 Ω and charge transfer resistance is 2.17 Ω.

References

[1] Pranoti, H. Patil, Vidya, V. Kulkarni, Sushilkumar A. Jadhav, Journal of Composites Science 6(12), 363 (2022); https://doi.org/10.3390/jcs6120363

[2] K. Ye, K. Li, Y. Lu, Z. Guo, N. Ni, H. Liu, Y. Huang, H. Ji, P. Wang, Trends in Analytical Chemistry,116,102-108 (2019); https://doi.org/10.1016/j.trac.2019.05.002

[3] S. Ariponnammal, S. Shalini, S. Anusha, Crystal Research and Technology, 57(11), 2200106 (2022); https://doi.org/10.1002/crat.202200106

[4] https://oqmd.org/materials/entry/1758603

[5] https://next-gen.materialsproject.org/materials/mp-4682?chemsys=Zn-Se-O

[6] A. Modwi, K. K. Taha, L. Khezami, Zeitschrift für Physikalische Chemie, 235, 745 (2021); https://doi.org/10.1515/zpch-2019-1473

[7] http://www.ejpau.media.pl/volume11/issue2/art-25.html

[8] Lee, Joo-Hee Kim, Chang-Il Paik, Jong-Hoo Cho, Jeong-Ho Jeong, Younghun Lee, Young-Jin

Nahm, Sahn, Journal of the Korean Institute of Electrical and Electronic Material Engineers, 24(11), 859-864 (2011); https://doi.org/10.4313/JKEM.2011.24.11.859

[9] Aparicio, Gladis Medina-Vargas, Giovanni Díaz-Puentes, Edgar, Heliyon, 6(11), e05262 (2020); https://doi.org/10.1016/j.heliyon.2020.e05262

[10] https://chemistnotes.com/analytical_chemistry/thermogravimetric-analysis-principle-instrumentation-and-reliable-application/#google_vignette

[11] https://resources.perkinelmer.com/lab-solutions/resources/docs/FAQ_Beginners-Guide-to-Thermogravimetric-Analysis_009380C_01.pdf

[12] I. Rashid, N. H. Daraghmeh, M. M. Al Omari, B. Z. Chowdhry, S. A. Leharne, H. A. Hodali, A. A. Badwan, Profiles of Drug Substances Excipients and Related Methodology, 36, 241-285 (2011); https://doi.org/10.1016/B978-0-12-387667-6.00007-5

[13] De la Fuente, José Luis Ruiz-Bermejo, Marta Salvan, Cesar Osuna-Esteban, Susana, Polymer Degradation and Stability, 96(5), 943-948 (2011); https://doi.org/10.1016/j.polymdegradstab.2011.01.033

[14] John F. Moulder, William F. Stickle, Peter E. Sobol, Kennetlf D. Bomben, Edited by Jill Chastain, Handbook of X-Ray Photoelectron Spectroscopy, Perkin-Elmer Corporation, USA (1992).

[15] https://xpsdatabase.com/zinc-zn-z30/

[16] Anshuman Sahai, Navendu Goswami, Ceramics International, 40(9), 14569-14578 (2014); https://doi.org/10.1016/j.ceramint.2014.06.041

[17] Mohsen Shenasa, Sudhaxar Sainkar, David Lichtman, Journal of Electron Spectroscopy and Related Phenomena, 40(4), 329-337 (1986); https://doi.org/10.1016/0368-2048(86)80043-3

[18] https://sites.cardiff.ac.uk/xpsaccess/reference/oxygen/

[19] H. Gupta, S. Chakrabarti, S.Mothkuri, B. Padya, T. N. Rao, P. K. Jain, Materials Today Proceedings, 26 , 20 (2020); https://doi.org/10.1016/j.matpr.2019.04.198

[20] V. Adimule, B. C. Yallur, M. Challa, R. S. Joshi, Heliyon, 7(12), e08541 (2021); https://doi.org/10.1016/j.heliyon.2021.e08541

[21] Gissawong, Netsirin Srijaranai, Supalax Boonchiangma, Suthasinee Uppachai, Pikaned Seehamart, Kompichit Jantrasee, Sakwiboon Moore, Eric Mukdasai, Siriboon, Microchimica Acta, 188, 208 (2021); https://doi.org/10.1007/s00604-021-04869-z

[22] S. Ariponnammal, N. G. Basil Ralph, S. Shanmugha Soundare, R. Jayavel, Nano, 19(5), 2450021 (2024); https://doi.org/10.1142/S1793292024500218

[23] Badar, Waqas Ali, Husna Brooker, Olivia Newham, Elis Snow, Tim Terrill, Nicholas Tozzi, Gianluca Fratzl, Peter Knight, Martin Gupta, Himadri, PLOS ONE, 17(9), e0273832, (2022); https://doi.org/10.1371/journal.pone.0273832

[24] Aranzales, D. Briliani, I. McCrum, I.T. Wijenberg, J.H.O.J. de Vooys, Arnoud Koper, Marc, Electrochimica Acta, 368, 137606 (2021); https://doi.org/10.1016/j.electacta.2020.137606

[25]https://batch.libretexts.org/print/url=https://chem.libretexts.org/Bookshelves/Analytical_Chemistry/Supplemental_Modules_%28Analytical_Chemistry%29/Analytical_Sciences_Digital_Library/Courseware/Analytical_Electrochemistry%3A_The_Basic_Concepts/04_Voltammetric_Methods/A._Basics_of_Voltammetry/02_Potential_Sweep_Methods/b%29_Cyclic_Voltammetry/ii%29_Important_parameters_in_CV.pdf

[26] https://www.nanoscience.com/techniques/electrochemistry/electrochemical-measurements-cyclic-voltammetry/

[27] K. V.Sankar, D . Kalpana, R. K. Selvan, Journal of Applied Electrochemistry, 42, 463 (2012); https://doi.org/10.1007/s10800-012-0424-2

[28] B.J. Reddy, P. Vickraman, A.S. Justin, Physica Status Solidi. 216(2), 1800595 (2018); https://doi.org/10.1002/pssa.201800595

[29] Y. Ge, X. Xie, J. Roscher, Q. Qu. Journal of Solid State Electrochemistry, 24, 3215-3230 (2020); https://doi.org/10.1007/s10008-020-04804-x

[30] S. Ratha, A.K. Samantara, Characterization and Performance Evaluation of Supercapacitor. In: Supercapacitor: Instrumentation, Measurement and Performance Evaluation Techniques. Springer Briefs in Materials. Springer, Singapore, 23-43 (2018); https://doi.org/10.1007/978-981-13-3086-5_3

[31]https://www.metrohm.com/content/dam/metrohm/shared/documents/application-notes/an-s/AN-SC-001.pdf

[32] B.A. Mei, O. Munteshari, J. Lau, B. Dunn, L. Pilon, Journal of Physical Chemistry C, 122(1), 194 (2018); https://doi.org/10.1021/acs.jpcc.7b10582

[33]https://partners.metrohm.com/GetDocumentPublic?action=get_dms_document&docid=2043973.

[34] W. Choi, H. C. Shin, J. M. Kim, J. Y. Choi, W. S. Yoon, Journal of Electrochemical Science and Technology, 11(1), 1-13 (2020); https://doi.org/10.33961/jecst.2019.00528

[35] E. P. Randviir, C. E. Banks, Analytical Methods, 5(5), 1098-1115 (2013); https://doi.org/10.1039/c3ay26476a

[36] Y. She, B. Tang, D. Li, X. Tang, J. Qiu, Z. Shang, W. Hu, Coatings, 8(10), 340 (2018); https://doi.org/10.3390/coatings8100340

[37] Ramesh Aravind Murugesan, Krishna Chandar Nagamuthu Raja, Nanotechnology 33(3), 035402(2021); https://doi.org/10.1088/1361-6528/ac2e24

[38] Ramesh Aravind Murugesan, C. Kalaiselvi, B. Revathi, A. Nirmala Grace,Sudhagar Pitchaimuthu, S. Suresh, V. Sindhu, Krishna Chandar Nagamuthu Raja, Nano, 16(12), 2150138 (2021); https://doi.org/10.1142/S1793292021501381

[39] Amit Kumar, Ashok Kumar, Ashavani Kumar, Solid State Sciences, 105, 106252 (2020); https://doi.org/10.1016/j.solidstatesciences.2020.106252

[40]https://www.cds.caltech.edu/~murray/books/AM05/wiki/FAQ:_What_does_the_Nyquist_plot_look_like_for_a_system_with_poles_at_the_origin.html

[41] https://en.wikipedia.org/wiki/Nyquist_stability_criterion

[42] https://chemistry.stackexchange.com/questions/165572/calculating-conductivity-from-nyquist-plot-plot-has-no-semi-circles

[43] https://scsolutions.com/wp-content/uploads/Theshapesofnyquistplots.pdf